Differential cross sections of double photoionization of lithium

A. S. Kheifets*
Research School of Physical Sciences, The Australian National University, Canberra, Australian Capital Territory 0200, Australia

D. V. Fursa and I. Bray
Institute of Theoretical Physics, Curtin University, Perth, Western Australia 6845, Australia

J. Colgan
Theoretical Division, Los Alamos National Laboratory, Los Alamos, New Mexico 87545, USA

M. S. Pindzola
Department of Physics, Auburn University, Auburn, Alabama 36849, USA
(Received 11 June 2010; published 3 August 2010)

We extend our previous application of the convergent close-coupling (CCC) and time-dependent close-coupling (TDCC) methods [Phys. Rev. A **81**, 023418 (2010)] to describe energy and angular resolved double photoionization (DPI) of lithium at arbitrary energy sharing. By doing so, we are able to evaluate the recoil ion momentum distribution of DPI of Li and make a comparison with recent measurements of Zhu *et al.* [Phys. Rev. Lett. **103**, 103008 (2009)].

DOI: 10.1103/PhysRevA.82.023403 PACS number(s): 32.80.Fb, 32.30.Rj, 32.70.−n, 31.15.ve

I. INTRODUCTION

Differential, with respect to the photoelectron energies and angles (or momenta), characterization of the double photoionization (DPI) process brings a wealth of information [1]. It allows for detailed analysis of various DPI mechanisms [2] and elucidation of the role of many-electron correlations [3]. On the experimental side, differential DPI measurements were greatly facilitated by the use of the cold target recoil ion momentum spectroscopy (COLTRIMS) technique [4]. On the theoretical side, various nonperturbative numerical methods were adopted to perform DPI calculations on a range of atomic and molecular targets with great accuracy and computational efficacy. In addition, extraction of the DPI amplitudes from measured differential cross sections [5,6] made possible a clear separation of essential dynamics of the DPI process and a much neater comparison between various theories and experiment.

Up to now, differential DPI cross sections and amplitudes have been established unambiguously for the simplest two-electron targets: the atomic helium and the molecular hydrogen. In the case of He, a broad consensus exists among various theories and experiment [1]. In the case of H_2, theoretical predictions [7,8] are consistent with the most accurate DPI measurements on the hydrogen molecule fixed in space [9,10].

Beyond these simplest targets, a comparison between the experiment and *ab initio* theory is more problematic. There have been a number of differential DPI measurements on complex atoms. Bolognesi *et al.* [11–13] reported fully resolved DPI cross sections of noble gas atoms. However, no adequate theoretical treatment was offered to these data. Only an empirical partial-wave analysis was performed for Ar $3p^6$ and the asymptotic or helium-like calculations were presented in the case of Ne $2s^2$. Another set of differential DPI measurements was performed on the alkaline-earth metal atoms Ca $4s^2$ [14–16] and Sr $5s^2$ [17,18]. However, theoretical interpretation of these data [19,20] involved some adjustable fitting parameters. There have been a number of theoretical reports of differential DPI cross sections of Be $2s^2$ [21–24]. However, only the total integrated cross section is known experimentally for this target [25–27].

Thus far, the lithium atom is the only many-electron target beyond He and H_2 for which both the theory and experiment can produce reliable differential cross sections. Theoretical-angular and energy-resolved triply differential cross sections (TDCS) were reported for Li by Kheifets *et al.* [28]. These authors [28] employed nonperturbative convergent close-coupling (CCC) and time-dependent close-coupling (TDCC) methods to describe the DPI of Li at the equal energy sharing. They introduced a set of symmetrized DPI amplitudes which parametrized conveniently the TDCS in the singlet and triplet channels. This formalism can be readily generalized to an arbitrary energy sharing, although the number of symmetrized DPI amplitudes should be doubled in this case. On the experimental side, Zhu *et al.* [29] performed differential measurements of Li DPI resolved with respect to the sum photoelectron momentum (or equivalently, the recoil ion momentum). Even though they were not able to resolve individual photoelectron momenta, a sum momentum measurement could provide important information on the propensity rules governing the two-electron escape as was demonstrated in the case of He by Knapp *et al.* [30].

To describe the recoil ion momentum distribution measured by Zhu *et al.* [29], a complete set of TDCS should be integrated across various energy sharings and mutual photoelectron angles. In the present work, we perform such a procedure using the recipe suggested by Pont and Shakeshaft [31]. Instead of direct integration, we parametrize the TDCS with a pair of symmetric and antisymmetric DPI amplitudes in the singlet and triplet channels (four amplitudes in total). We perform calculations of these amplitudes at several selected energy sharings and then interpolate the amplitudes across the whole

*A.Kheifets@anu.edu.au

interval of the excess energy. Then the recoil ion momentum distribution can be readily evaluated.

The rest of the paper is organized as follows. In Secs. II A and II B, we give a brief summary of the CCC and TDCC methods. An evaluation of the symmetrized DPI amplitudes and the recoil ion momentum distribution is described in Secs. II C and II D. Numerical results are presented in Sec. III. We conclude in Sec. IV by discussing the similarities and differences of predictions of the two theoretical models and the experiment.

II. FORMALISM

A. CCC method

The application of the CCC method to DPI of Li is described in detail in our earlier publications [28,32]. In brief, the ionization amplitude is written as the matrix element of the dipole operator between the multiconfiguration initial state and the final multichannel state. The latter is expanded over the set of channel states, each of which is a product of the Li^+ ion target state $\langle 0,1\|\alpha\rangle$ and a distorted wave $\langle 2\|kl\rangle$. The target electrons are labeled 0,1 and the continuum electron is tagged 2. The core electron 0 is frozen to the $1s$ ground state. The label $\alpha \equiv NLS$ comprises the integer N which numbers the set of target states with the given orbital momentum L and spin S. The negative energy target states $\mathcal{E}_\alpha < 0$ are attributed to single photoionization whereas the positive energy states $\mathcal{E}_\alpha > 0$ contribute to DPI.

The interelectron interaction is accounted for in the CCC method to infinite order. This is achieved by integrating the bare dipole matrix element with the scattering T matrix

$$D_{\alpha l}(\kappa) = d_{\alpha l}(\kappa) + \sum_{\alpha' l'} \sum\!\!\!\!\!\!\int_{\kappa'} \frac{\langle \alpha l \kappa \,\|T\|\, \alpha' l' \kappa'\rangle \; d_{\alpha' l'}(\kappa')}{E - \kappa'^2/2 - \mathcal{E}_{\alpha'} + i\delta}. \qquad (1)$$

Here κ and l denote the linear and angular momenta of the continuous electron state and $E = \kappa^2/2 + \mathcal{E}_\alpha$ is the total energy of the scattering system which consists of the photoelectron and the Li^+ ion. The bare dipole matrix elements $d_{\alpha l}(\kappa)$ are expressed via radial integrals containing the ground and final state orbitals and the dipole operator either in the length $\sum_{j=1}^{3} r_j$ or velocity $\omega^{-1}\sum_{j=1}^{3}\nabla_j$ gauges. The velocity gauge proved to be more accurate in CCC calculations of DPI on Li and we will be using it in the present work.

The reduced dipole matrix element Eq. (1) is used to construct the DPI matrix element which corresponds to ejection of the photoelectron pair with the linear momenta k_1,k_2, and the angular momenta l_1,l_2

$$D_{S l_1 l_2}(k_1,k_2) = (-i)^{l_1+l_2}\, e^{i[\sigma_{l_1}(Z=2)+\sigma_{l_2}(Z=1)]} D_{\alpha l_2}(k_2)\, \langle l_1 k_1, 1s \,\|\, \alpha\rangle. \qquad (2)$$

Here $\langle l_1 k_1, 1s \,\|\, \alpha\rangle$ is the radial projection of the positive energy target state α of the matching energy $\mathcal{E}_\alpha = k_1^2/2$ to the final ionized state. The latter state is composed of the photoelectron $l_1 k_1$ and the bound electron frozen to the $1s$ state. The Coulomb scattering phases $\sigma_{l_2}(Z=1)$ and $\sigma_{l_1}(Z=2)$ depend on the asymptotic charge of the singly and doubly charged ions, respectively.

The spin S in Eq. (2) is related to the positive energy target state $\langle 0,1|\alpha\rangle$, $\alpha \equiv NLS$. It is physically more transparent to redefine matrix elements (2) with respect to the spin of the photoelectron pair 1,2

$$F_{S l_1 l_2}(k_1,k_2) = \sum_{S'=0,1} [(-1)^{S'} D_{S' l_1 l_2}(k_1,k_2) + D_{S' l_2 l_1}(k_1,k_2)\gamma_{SS'}]. \qquad (3)$$

The recoupling coefficients $\gamma_{SS'}$ are given by Eqs. (32) and (33) of Stelbovics *et al.* [33] in the case of equal energy sharing and by Eqs. (34) and (35) in the case of an arbitrary energy sharing.

The matrix elements (2) are then fed to the following expression for the TDCS which takes the form of the partial wave expansion:

$$\frac{d^3\sigma}{d\Omega_1 d\Omega_2\, dE_2} = C \sum_{S=0,1} \left| \sum_{l_1 l_2} \boldsymbol{e}\cdot \mathcal{Y}_1^{l_1 l_2}(\boldsymbol{n}_1,\boldsymbol{n}_2)\; F_{S l_1 l_2}(k_1,k_2) \right|^2. \qquad (4)$$

Here $C = 8\pi^2\omega/(3c)$ is the photoionization constant and $c \simeq 137$ is the speed of light in atomic units. The unit vectors $\boldsymbol{n}_i = \boldsymbol{k}_i/k_i, i = 1,2$ are directed along the photoelectron momenta, $\boldsymbol{e}$ is the polarization vector of light. The bipolar harmonics are tensors of rank 1 expressed by the following tensorial product [34]:

$$\mathcal{Y}_1^{l_1 l_2}(\boldsymbol{n}_1,\boldsymbol{n}_2) = Y_{l_1}(\boldsymbol{n}_1) \otimes Y_{l_2}(\boldsymbol{n}_2). \qquad (5)$$

B. TDCC method

A description of the TDCC approach to DPI of Li was recently presented [28,35]. Briefly, two calculations are made, one for the two photoelectrons coupling to a singlet state, and one for both photoelectrons coupling to a triplet state. After propagation of the Schrödinger equation, one can obtain the final momentum-space amplitudes using

$$P_{l_1 l_2}^{LS}(k_1,k_2,T) = \int_0^\infty dr_1 \int_0^\infty dr_2 P_{k_1 l_1}(r_1) P_{k_2 l_2}(r_2) P_{l_1 l_2}^{LS}(r_1,r_2,T), \qquad (6)$$

where the box-normalized radial distorted-waves P_{kl} are solutions of the one-electron radial Schrödinger equation [35]. The final time solutions $P_{l_1 l_2}^{LS}(r_1,r_2,T)$ are obtained by propagating the Schrödinger equation for the correlated two-electron radial wave function with the total orbital momentum L and spin S to sufficiently long times $t = T$.

TDCS may then be calculated from these amplitudes using the expression [36]

$$\frac{d^3\sigma}{dE_2 d\Omega_1 d\Omega_2} = 2\frac{1}{k_1 k_2}\frac{\omega}{I}\frac{\partial}{\partial t}\int_0^\infty dk_1 \int_0^\infty dk_2 \delta\left[\beta - \tan^{-1}\left(\frac{k_2}{k_1}\right)\right] \times \sum_{S=0,1} w_S \left| \sum_{l_1,l_2} (-i)^{l_1+l_2} e^{i(\sigma_{l_1}+\sigma_{l_2})} e^{i(\delta_{l_1}+\delta_{l_2})} \times P_{l_1 l_2}^{LS}(k_1,k_2,t)\, \boldsymbol{e}\cdot \mathcal{Y}_L^{l_1 l_2}(\boldsymbol{n}_1,\boldsymbol{n}_2) \right|^2, \qquad (7)$$

where β is the hyperspherical angle between k_1 and k_2, I is the radiation field intensity, σ_l and δ_l are the Coulomb and

distorted-wave phases, respectively, and integration over all solid angles and ejected energy gives the total integral cross section. This expression includes the appropriate spin statistical factors [35] w_S, where $w_0 = 1/4$ and $w_1 = 3/4$. The factor of 2 results from the initial occupation number of the $1s$ orbital. All TDCC calculations presented in this paper were made in the length gauge, and test calculations made in the velocity gauge were almost identical to the calculations presented here.

C. Symmetrized DPI amplitudes

As was shown in our previous work [28], TDCS expressions (4) and (7) can be written in the form

$$\frac{d^3\sigma}{d\Omega_1 d\Omega_2\, dE_2} = \sum_{S=0,1} \left| [\boldsymbol{e}\cdot\boldsymbol{n}_1 + (-1)^S\, \boldsymbol{e}\cdot\boldsymbol{n}_2]\, \mathcal{M}_S^g(k_1,k_2,\theta_{12}) + [\boldsymbol{e}\cdot\boldsymbol{n}_1 - (-1)^S\, \boldsymbol{e}\cdot\boldsymbol{n}_2]\, \mathcal{M}_S^u(k_1,k_2,\theta_{12}) \right|^2, \quad (8)$$

in which the trivial kinematic dependence of the escape directions $\boldsymbol{n}_1, \boldsymbol{n}_2$ relative the polarization vector $\boldsymbol{e}$ is separated from the essential dynamics of the DPI process. These dynamics are contained in a pair of the symmetric *gerade* (g) and antisymmetric *ungerade* (u) DPI amplitudes

$$\mathcal{M}_S^{g/u}(k_1,k_2,\theta_{12}) = \frac{\sqrt{3C}}{4\pi} \sum_{l=0}^{\infty} \frac{(-1)^l}{\sqrt{l+1}} [P'_{l+1}(x) \mp (-1)^S P'_l(x)] \times F^{\pm}_{Sll+1}(k_1,k_2), \quad (9)$$

where $x = \cos\theta_{12} = \boldsymbol{n}_1 \cdot \boldsymbol{n}_2$. These amplitudes satisfy the following exchange symmetry:

$$\begin{aligned} \mathcal{M}_S^g(k_1,k_2,\theta_{12}) &= \mathcal{M}_S^g(k_2,k_1,\theta_{12}), \\ \mathcal{M}_S^u(k_1,k_2,\theta_{12}) &= -\mathcal{M}_S^u(k_2,k_1,\theta_{12}), \\ \mathcal{M}_S^u(k_1 = k_2,\theta_{12}) &= 0. \end{aligned} \quad (10)$$

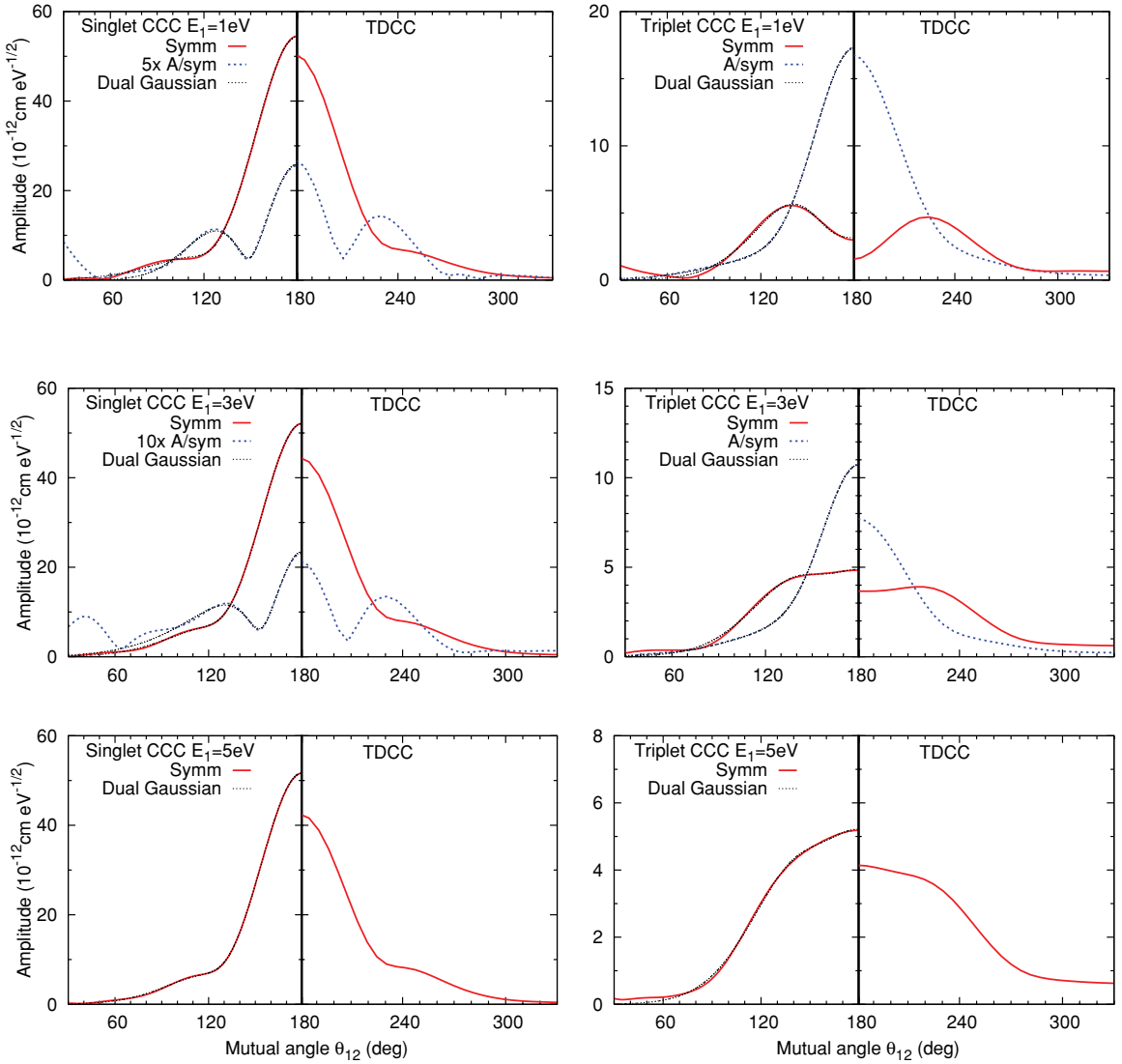

FIG. 1. (Color online) Moduli of the symmetrized DPI amplitudes of Li at the photon energy $\omega = 91$ eV and various energy sharings $E_1 : E_2 = 1:9$, $3:7$, and $5:5$ eV. Each panel is split in two at the folding symmetry point $\theta_{12} = \pi$. The left half of the panel accommodates the CCC amplitudes whereas the right half displays the TDCC amplitudes. The symmetric and antisymmetric amplitudes are shown with red solid and blue dashed lines, respectively, in the singlet (left) and triplet (right) columns of plots. The dual Gaussian fit to the CCC amplitudes is shown with thin dotted lines.

Thus only a pair of symmetric amplitudes $\mathcal{M}^{g}_{S=0,1}(k_1 = k_2,\theta_{12})$ are needed to describe the angular distribution of photoelectrons in DPI of Li at equal energy sharing. Two pairs of amplitudes are needed in an arbitrary energy sharing case.

D. Recoil ion momentum distribution

In this section, we follow the derivation of Pont and Shakeshaft [31]. We streamline the notations and write Eq. (8) as

$$\frac{d^3\sigma}{d\Omega_1 d\Omega_2\, dE_2} = \sum_{S=0,1} |f_S(\boldsymbol{k}_1,\boldsymbol{k}_2)|^2, \tag{11}$$

where

$$\begin{aligned} f_S(\boldsymbol{k}_1,\boldsymbol{k}_2) &= f_S(k_1,k_2,x)\,\boldsymbol{k}_1\cdot\boldsymbol{e} + f_S(k_2,k_1,x)\,\boldsymbol{k}_2\cdot\boldsymbol{e} \\ &= g^{+}_S(p,k,y)\,\boldsymbol{p}\cdot\boldsymbol{e} + g^{-}_S(p,k,y)\,\boldsymbol{k}\cdot\boldsymbol{e}. \end{aligned} \tag{12}$$

Here we returned to nonsymmetrized amplitudes $f_S(k_i,k_j,x)$, which are expressed via symmetrized amplitudes (9) as

$$\begin{aligned} f_S(k_1,k_2,x) &= \mathcal{M}^{g}_S(k_1,k_2,x) + \mathcal{M}^{u}_S(k_1,k_2,x), \\ f_S(k_2,k_1,x) &= \mathcal{M}^{g}_S(k_1,k_2,x) - \mathcal{M}^{u}_S(k_1,k_2,x). \end{aligned} \tag{13}$$

In Eq. (12) we also introduced the sum $\boldsymbol{p} = \boldsymbol{k}_1 + \boldsymbol{k}_2$ and difference $\boldsymbol{k} = \boldsymbol{k}_1 - \boldsymbol{k}_2$ momenta and their respective amplitudes

$$g^{\pm}_S(p,k,y) = \frac{1}{2}\left[\frac{f_S(k_1,k_2,x)}{k_1} \pm \frac{f_S(k_2,k_1,x)}{k_2}\right], \tag{14}$$

where $y = \boldsymbol{p}\cdot\boldsymbol{k}/(pk)$. Further on, we make the following Legendre polynomial expansions:

$$|g^{\pm}_S(p,k,y)|^2 = \sum_l (2l+1) I^{\pm}_{lS}(p)\, P_l(y),$$

$$\mathrm{Re}\{g^{+}_S(p,k,y)[g^{-}_S(p,k,y)]^*\} = \sum_l (2l+1) J_{lS}(p)\, P_l(y).$$

Here the plus, minus, and mixed momenta are

$$\begin{aligned} I^{\pm}_{lS} &= \frac{1}{2}\int_{-1}^{1} |g^{\pm}_S(k_1,k_2,y)|^2 P_l(y)\, dy, \\ J_{lS} &= \frac{1}{2}\int_{-1}^{1} 2\mathrm{Re}\{g^{+}_S(k_1,k_2,y)[g^{-}_S(k_1,k_2,y)]^*\} P_l(y)\, dy. \end{aligned} \tag{15}$$

With these notations, the sum momentum distribution is given by the following differential cross section:

$$\frac{d^2\sigma}{dp\, d\Omega_p} = \frac{1}{4\pi}\sum_{S=0,1}\frac{d\sigma_S}{dp}[1 + \beta_S P_2(\cos\theta_p)], \tag{16}$$

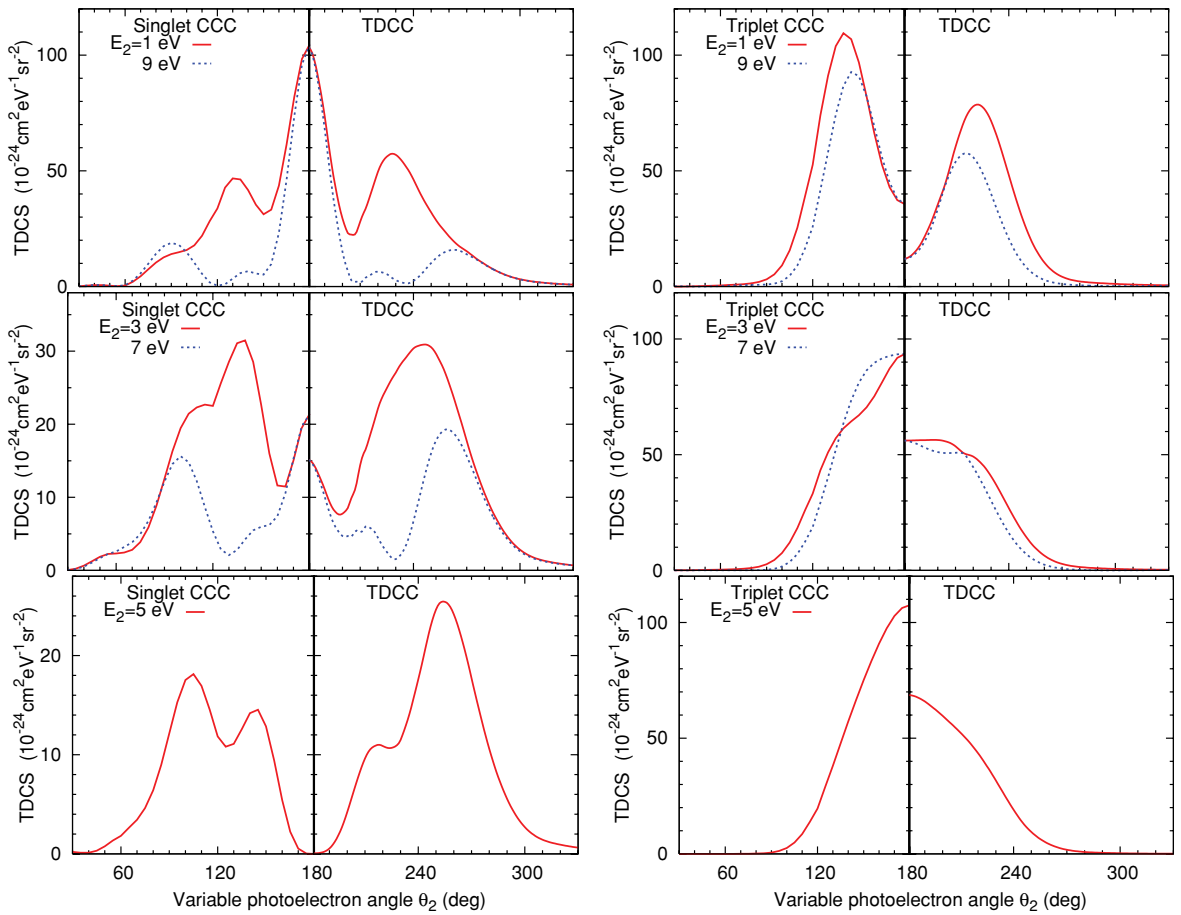

FIG. 2. (Color online) The TDCS of DPI of Li at $\omega = 91$ eV for the coplanar kinematics and fixed photoelectron angle $\theta_1 = 0^\circ$ as a function of the variable angle θ_2. The energy of the variable angle photoelectron E_2 is indicated on each panel.

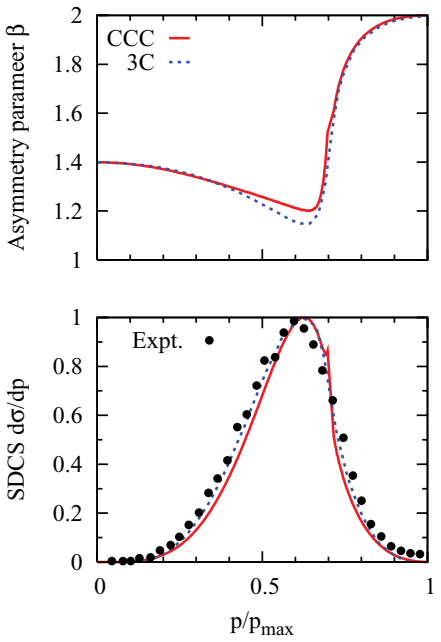

FIG. 3. (Color online) The recoil ion momentum distribution following DPI of He at $\omega = 99$ eV. The asymmetry β parameter (top) and the normalized SDCS $d\sigma/dp$ (middle) are plotted versus the sum momentum $p/p_{\max}$ measured as a fraction of the maximum available momentum. The present CCC results (red solid line) are plotted along with the 3C calculation (blue dashed line) and the experimental data (dots) from Ref. [31].

where the asymmetry parameter and the single differential, with respect to the momentum, cross section (SDCS) are given by the following expressions:

$$\beta_S = 2\,\frac{p^2 I_{0S}^{+}(p) + k^2 I_{2S}^{-} + kpJ_{1S}(p)}{p^2 I_{0S}^{+}(p) + k^2 I_{0S}^{-} + kpJ_{1S}(p)},$$
$$\frac{d\sigma_S}{dp} = kp^2[p^2 I_{0S}^{+}(p) + k^2 I_{0S}^{-}(p) + kpJ_{1S}(p)]. \tag{17}$$

The spin index in Eqs. (16) and (17) corresponds to the spin of the amplitudes (12) and (14).

In the asymptotic limits $p \to 0$ or $k \to 0$, the asymmetry β parameters can be found analytically. Indeed, these limits correspond to the antiparallel or parallel escapes of the two equal energy photoelectrons (i.e., $x = \mp 1$ for all the y values). So the amplitudes $f_S(k_1,k_2,x)$ entering integrals (15) via Eq. (14) can be taken outside the integration sign. The residual parts of the integrals are then evaluated analytically. This procedure leads to the following limits:

$$p \to 0 \begin{cases} \beta_{S=0} \to 7/5 \\ \beta_{S=1} \to 0 \end{cases},$$
$$k \to 0 \begin{cases} \beta_{S=0} \to 2 \\ \beta_{S=1} \to 2 \end{cases}. \tag{18}$$

The experimentally measured SDCS is given by the spin sum $d\sigma/dp = \sum_S d\sigma_S/dp$. Another momentum distribution which can be determined experimentally is the double differential cross section (DDCS)

$$\frac{d\sigma}{dp_x dp_z} = \int_{-p_{\max}}^{p_{\max}} dp_y \frac{d\sigma}{dp_x dp_y dp_z} = \int_{-p_{\max}}^{p_{\max}} dp_y \frac{1}{p^2}\frac{d\sigma}{dp d\Omega_p}, \tag{19}$$

where $p_{\max} = \sqrt{p^2 - p_x^2 - p_z^2} = \sqrt{p^2 - p_\parallel^2}$. It reflects the momentum distribution projected onto the detection plane which contains the polarization axis of light $\boldsymbol{e} \| \hat{\boldsymbol{z}}$.

III. RESULTS

The experimental data reported by Zhu *et al.* [29] were taken at the two fixed, photon energies of $\omega = 85$ and 91 eV, which corresponded to the excess energies of 4 and 10 eV above the DPI threshold. To match these data, we performed our calculations at the same set of photon energies.

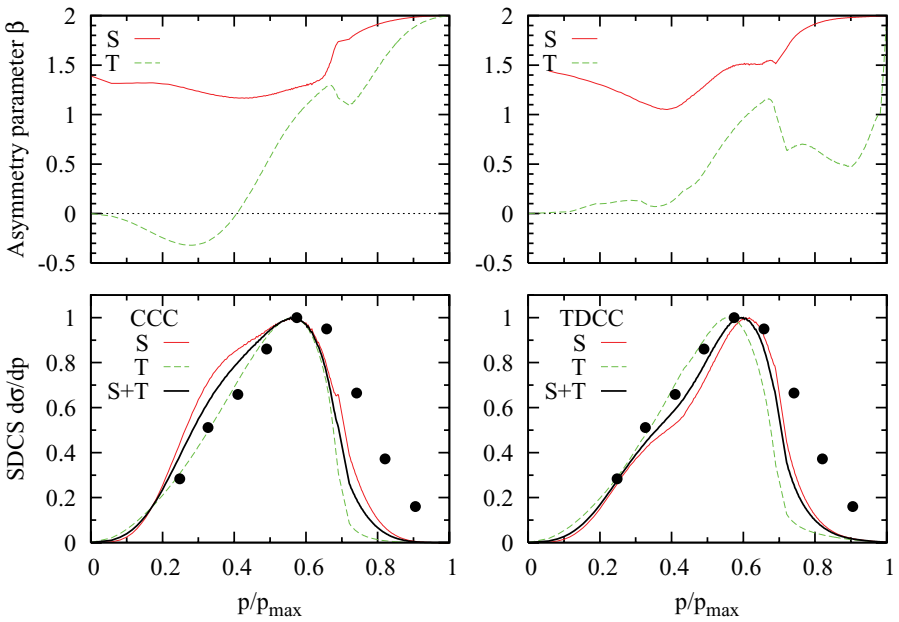

FIG. 4. (Color online) The recoil ion momentum distribution of the DPI of Li at $\omega = 91$ eV. The asymmetry parameter β (top) and the SDCS normalized to 1 at its maximum (bottom) in the singlet (S, red solid line) and triplet (T, green dashed line) channels plotted versus the the sum momentum $p/p_{\max}$ measured as a fraction of the maximum available momentum. The spin summed SDCS on the bottom panel (S + T, thick black solid line) are compared with the experiment [29].

A. Symmetrized DPI amplitudes

The moduli of the symmetrized DPI amplitudes (9) at the photon energy of $\omega = 91$ eV and various energy sharings are displayed in Fig. 1. The three rows of plots display the amplitudes for the slow photoelectron energies fixed at $E_1 = 1$, 3, and 5 eV (from top to bottom). The left column contains the singlet amplitudes whereas the right column displays the triplet amplitudes. The amplitudes are plotted as functions of the mutual photoelectron angle θ_{12}. As such, they are symmetric relative to $\theta_{12} = \pi$. We use this symmetry and plot two sets of amplitudes on the same graph: the CCC amplitudes are displayed for $\theta_{12} \leqslant \pi$ and the TDCC amplitudes are drawn for $\theta_{12} \geqslant \pi$. This way the difference between the two sets of amplitudes is clearly seen. There are two amplitudes, symmetric and antisymmetric, in the singlet and triplet channels. The only exception is the equal energy sharing case $E_1 = E_2 = 5$ eV shown on the bottom row of plots which contain only symmetric amplitudes.

It is customary to fit the moduli of the symmetrized amplitudes with a Gaussian ansatz. The amplitudes displayed in Fig. 1 are clearly non-Gaussian. To fit these amplitudes, we applied a dual Gaussian ansatz which includes a mixture of two Gaussians with a relative phase shift

$$G(t) = A_1 \exp\left(-t^2/2\Gamma_1^2\right) + e^{i\phi} A_2 \exp\left(-t^2/2\Gamma_2^2\right). \quad (20)$$

Here $t = \pi - \theta_{12}$ and Γ are related to the full width at half maximum $\Delta\theta_{12} = \Gamma\sqrt{8\ln 2}$. The physical rationale of the dual Gaussian ansatz is the following. In the CCC formalism, DPI is considered as a two-stage process in which the primary photoelectron knocks out the secondary photoelectron via inelastic collision with the singly ionized target. Kheifets and Bray [3] related the Gaussian width parameter with the momentum profile of the corresponding target orbital bound to the singly charged ion. For heteroshell targets such as Li, there are two orbitals $1s$ and $2s$ involved in this process. Therefore it is logical to introduce two Gaussian width parameters corresponding to each of these orbitals. More detailed analysis of the DPI process in heteroshell atomic targets will be performed elsewhere [37].

We used the five parameters $A_{1,2}$, $\Gamma_{1,2}$, and ϕ to fit the CCC amplitudes in Fig. 1. The quality of the fit is so good that the dual Gaussian ansatz can only be distinguished from the CCC amplitude for very small interelectron angles where the raw amplitude may exhibit some unphysical "tails."

Agreement between the CCC and TDCC calculations is generally good. Except for some mismatch of the height of the amplitudes, the TDCC amplitudes tend to be slightly more extended toward small mutual angles as compared to their CCC counterparts.

B. Fully resolved TDCS

In Fig. 2 we present the TDCS calculated at the photon energy $\omega = 91$ eV for the coplanar kinematics and various energy sharings between the two photoelectrons. The angle of one of the photoelectrons is fixed at $\theta_1 = 0^\circ$ along the polarization axis of light. In these kinematics, general TDCS

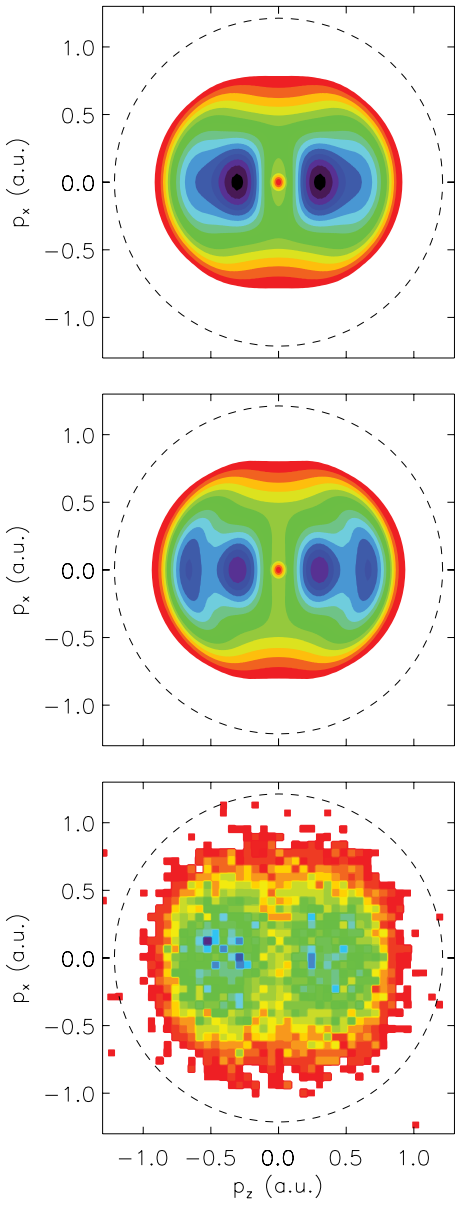

FIG. 5. (Color online) The DDCS $d^2\sigma/dp_x\,dp_z$ of the DPI of Li at the photon energy of $\omega = 91$ eV. The three panels (from top to bottom) display the CCC calculation, the TDCC calculation, and the experiment [38]. The dashed circle on each panel indicates the maximum available recoil momentum $p_{\max} = 1.21$ a.u.

expression (8) is simplified to

$$\frac{d^3\sigma(\theta_1 = 0)}{d\Omega_1 d\Omega_2\, dE_2} = \sum_{S=0,1} \left|[1 + (-1)^S \cos\theta_2]\, \mathcal{M}_S^g(\theta_2) + [1 - (-1)^S \cos\theta_2]\, \mathcal{M}_S^u(\theta_2)\right|^2. \quad (21)$$

Both the kinematics factors and the amplitudes entering Eq. (21) are symmetric with respect to the angle $\theta_2 = 180^\circ$ which allows us to accommodate two sets of data, the CCC and TDCC, on the same plot as in Fig. 1.

The TDCS at three energy sharings between the slow and fast photoelectrons 1 : 9, 3 : 7, and 5 : 5 eV are shown in Fig. 2 (from top to bottom). These three sets of TDCS are generated using the symmetrized DPI amplitudes displayed in

the matching panels of Fig. 1. These amplitudes correspond to the energy sharing in which $E_1 \leqslant E_2$. To generate the TDCS at the complementary energy sharing $E_1 > E_2$ we used the exchange symmetry relation (10).

First, we analyze the singlet TDCS. At the very uneven energy sharing of 1:9 eV, the angular distributions of both the slow and fast photoelectrons have a strong peak at 180° which corresponds to the back-to-back emission for the presently fixed photoelectron angle of zero degrees. This peak originates from the asymmetric amplitude $\mathcal{M}^u_{S=0}$ as the kinematic factor accompanying the symmetric amplitude $\mathcal{M}^g_{S=0}$ is zero at the back-to-back emission. That is why the height of this peak is identical both for the fast and slow photoelectrons. As the energy sharing becomes more even (from the top left to the bottom left panels of Fig. 2), the back-to-back peak gradually declines until it disappears completely at the equal energy sharing where the asymmetric amplitude is zero. The magnitude of the TDCS in the singlet channel is largest at a very asymmetric energy sharing (the top left panel) when the back-to-back escape is favored both by the kinematic and the dynamic amplitude factors. Conversely, at the equal energy sharing (the bottom left panel) the magnitude of the singlet TDCS is the smallest as the kinematic and the dynamic factors have to negotiate a compromise at an angle close to 120°.

In the triplet channel (the right column of Fig. 2), the evolution of the TDCS with the energy sharing is not so dramatic. As follows from Eq. (21), the symmetric amplitude is the main contributor to the TDCS. This amplitude shows little variation in magnitude as is seen from the right column of Fig. 1. However, this amplitude changes its shape considerably, displaying a noticeable minimum in the back-to-back direction at very asymmetric energy sharing. This minimum corresponds to the strong dip in the triplet TDCS at 180° (the top right panel). As the triplet symmetric amplitude flattens (middle and bottom right panels of Fig. 1), the corresponding TDCS display the strong maximum in the back-to-back emission. At all energy sharings, the contribution of the antisymmetric amplitude is small in the triplet channel. That is why the TDCS of the slow and fast photoelectrons are rather similar. The singlet and triplet TDCS are on par at a very uneven energy sharing, but the triplet channel gradually takes over toward the equal energy sharing. This is despite the fact that the singlet amplitude is much larger on the bottom panel of Fig. 1 than its triplet counterpart. This seeming contradiction is due to the different interplay between the dynamic and kinematic factors in the singlet and triplet channels.

The variation in amplitudes of Fig. 1 between the CCC and TDCC methods translates itself into the different TDCS of Fig. 2. This difference is, however, not qualitative, but rather quantitative, found in the relative peak heights of the corresponding TDCS. In the singlet channel, the difference between the CCC and TDCC is most profound for the smallest TDCS corresponding to the equal energy sharing (the bottom left panel). In the triplet channel, the CCC calculation produces systematically larger TDCS. This was already acknowledged in our previous paper [28], in which we analyzed the case of the equal energy sharing.

C. Recoil ion momentum distribution

The computational procedure outlined in Sec. II D requires knowledge of the DPI amplitudes at all possible energy sharings. In practice, the CCC amplitudes are calculated on a rather sparse energy grid to reduce the computation time to the minimum. To reconcile these contradictory requirements, we came up with the following computational strategy. We fitted raw DPI amplitudes with the dual Gaussian ansatz (20) at a few selected reference energy points and then extrapolated the parameters $A_{1,2}$, $\Gamma_{1,2}$, and ϕ by the polynomial fit across the whole energy range. To determine how well this procedure actually works and how sparse the reference energy grid can be, we performed a set of test calculations of the recoil ion momentum distribution corresponding to the DPI of the ground state He at $\omega = 99$ and 20 eV excess energy. These data are shown in Fig. 3 where we display the asymmetry β parameter (top) and the SDCS $d\sigma/dp$ (bottom) plotted versus the the sum

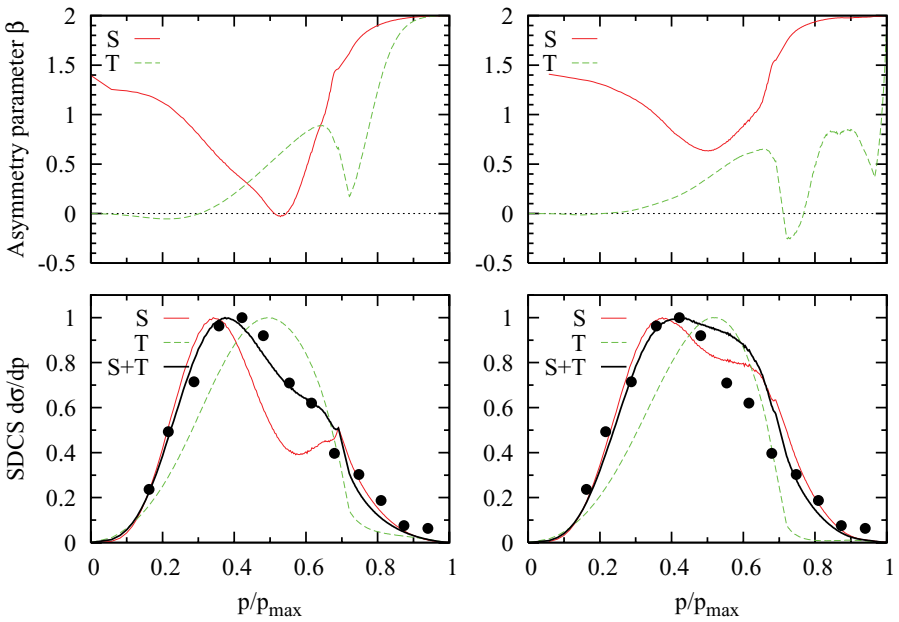

FIG. 6. (Color online) Same plots as in Fig. 4 for the photon energy $\omega = 85$ eV.

momentum $p/p_{\max}$ measured as a fraction of the maximum available momentum. The SDCS is normalized to unity in its maximum. The present CCC results (red solid line) are plotted along with the 3C calculation (blue dashed line) and the experimental data (dots) from Ref. [31]. Agreement between the two calculations and the experimental data (only available for the SDCS) is excellent, which validates our computation procedure.

The helium test case presented in Fig. 3 contains only one singlet channel. On the other hand, the corresponding Li data exhibited in Fig. 4 display two sets of the asymmetry β parameters (top panels) and the SDCS $d\sigma/dp$ (bottom panel) corresponding to the singlet (S) and triplet (T) channels. The spin summed (S+T) SDCS is also shown on the bottom panels and compared with experimental data of Zhu *et al.* [29]. The CCC and TDCC results are displayed in the left and right columns, respectively. The TDCC amplitudes could be calculated on a very fine energy mesh and used directly in the recoil momentum calculation. No additional interpolation was needed in this case.

As is seen from Fig. 4, the asymmetry β parameters clearly adhere to the asymptotic limits (18). However, at intermediate values of the sum momentum, the CCC and TDCC methods predict quite different sets of asymmetry parameters. In the TDCC calculation, $\beta_{S=1}$ data display a sharp turn at large $p/p_{\max} \sim 1$, whereas the CCC calculation returns a negative value of this parameter at $p/p_{\max} \sim 0$. The difference between the two sets of calculations is not so dramatic for the SDCS $d\sigma/dp$, especially when the summation over the spins is performed. Both calculations predict the spin summed SDCS which is quite close to the experiment [29]. One notable exception is the large values of the sum momentum $p/p_{\max} \sim 1$ where both calculations predict the SDCS well below the experimental values. This region of the sum momentum corresponds to the parallel escape of the two photoelectrons with equal energy sharing. As is seen from the bottom right panel of Fig. 2, this escape is suppressed in both calculations, though somewhat stronger in the CCC model. This suppression can be ultimately traced back to the symmetrized DPI amplitudes exhibited on the bottom panels of Fig. 1.

The difference between the CCC and TDCC calculations is seen more clearly in the DDCS plots presented in Fig. 5. Both theories predict the photoelectron angular distribution in the p_x, p_z plane extended along the polarization axis of light (horizontal in the figure). However, the CCC calculation predicts a single maximum in both $\pm p_z$ directions whereas the TDCC calculation shows a more complicated split maximum pattern. The origin of this pattern is most likely due to the sharp turn by $\beta_{S=1}$ in the interval of the sum momenta where $d\sigma/dp$ is still large. The presently available experimental data [38] (bottom panel of Fig. 5) have insufficient statistics to discriminate between the two calculations. However, the general shape of the DDCS is similar in the theory and experiment.

An analogous set of data is shown Figs. 6 and 7 for the photon energy of $\omega = 85$ which corresponds to the excess energy of 4 eV. As is seen from Fig. 6, the two calculations predict qualitatively similar sets of asymmetry β parameters and the SDCS. In comparison with the experiment [29], the

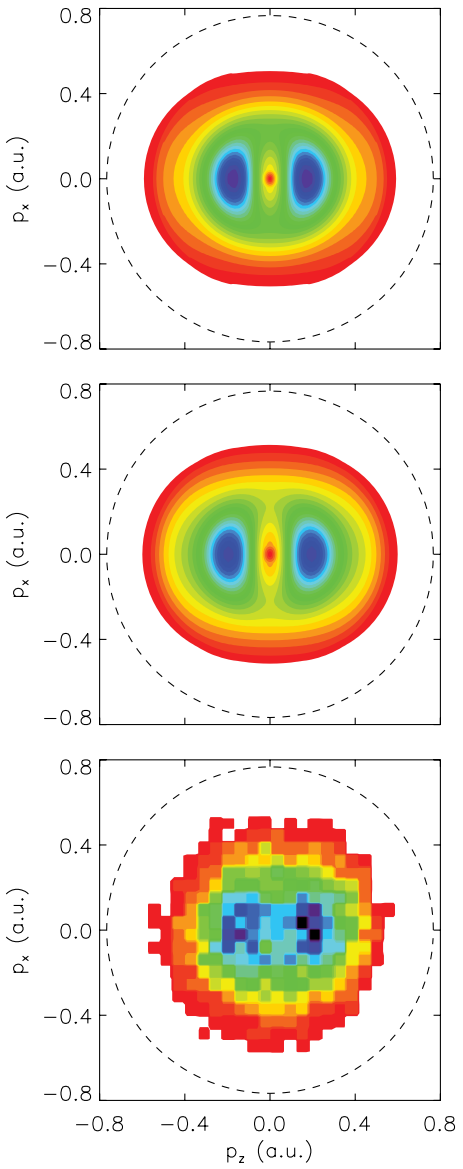

FIG. 7. (Color online) Same as Fig. 5 for the photon energy of $\omega = 85$ eV. The experimental data (bottom panel) are from Ref. [29]. The dashed circle on each panel indicates the maximum available recoil momentum $p_{\max} = 0.77$ a.u.

CCC calculation for the SDCS tend to be somewhat closer at intermediate values of $p/p_{\max}$. When the DDCS are compared in the two calculations and the experiment in Fig. 7, they all look quite similar. The calculated DDCS are somewhat more elongated in the polarization direction.

IV. CONCLUSION

In the present paper, we performed CCC and TDCC calculations of the fully resolved triply differential cross section (TDCS) of DPI of Li. Both numerical methods have been tested before in obtaining the total integrated cross sections (TICS) of the same process for which they produced very similar results across a wide range of photon energies [32,35]. Also, we verified our numerical schemes in a pilot calculation of the TDCS for the equal energy sharing between the photoelectrons

$E_1 = E_2 = 5$ eV [28]. In the present work, we extended our calculations to obtain TDCS at arbitrary energy sharing. This enabled us to reproduce the recoil ion momentum distribution and to make a comparison with the recently published [29] and still unpublished [38] experimental data.

The key ingredient of our computations is a set of symmetrized DPI amplitudes. These amplitudes were calculated on a sufficiently fine energy mesh in the TDCC method. As an alternative, in the CCC computation, the raw amplitudes were calculated on a rather sparse energy grid. This reference set of amplitudes was fitted with a generalized dual Gaussian ansatz. The fitting coefficients were then interpolated across the whole range of the excess energy. This procedure provided a complete description of the DPI process.

When we compared our calculated recoil ion momentum distributions, reasonable agreement with the experiment was found. At the photon energy $\omega = 91$ eV, both theories predict the SDCS which is quite close to the experimental data. However, the experimental SDCS extends much further toward $p/p_{\max} \sim 1$. This area of the sum momentum corresponds to the close-to-parallel emission of the equal energy photoelectrons. This emission pattern is suppressed in theory especially. At the photon energy $\omega = 85$ eV, both the CCC and TDCC calculations predict SDCS which are quite close to the experiment. The doubly differential, with respect to the p_x and p_z components of the sum momentum, cross section (DDCS) reflects the recoil ion momentum distribution in the detection plane which contains the polarization axis of light. Both the theories and experiment have the same pattern of the DDCS which is extended along the polarization axis direction.

The largest difference between the two models is reflected in the angular asymmetry β parameters recorded separately in the singlet and triplet channels. This difference can be traced back to the symmetrized DPI amplitudes which have a systematically larger angular span in the TDCC as compared to CCC. This difference is visible in the DDCS pattern which is quite different for the two models at $\omega = 91$ eV. Unfortunately, the experimental data have insufficient statistics to discriminate between the calculations.

We hope that our report will stimulate further energy and angular differential studies of the DPI of Li. The physics of this process is rich due to the interplay between the singlet and triplet channels, which is most revealing at arbitrary energy sharing between the photoelectrons. In the recoil ion channel, the spin-resolved momentum distribution display a very involved and nontrivial pattern. It would be also interesting to test theoretical predictions by differential detection of both photoelectrons, as is currently planned. This would provide discrimination between the two theoretical approaches, the CCC and TDCC, employed in the present study.

ACKNOWLEDGMENTS

We thank Alex Dorn for critical reading of the manuscript and supplying experimental data in numerical form.

The Los Alamos National Laboratory is operated by Los Alamos National Security, LLC for the National Nuclear Security Administration of the US Department of Energy under Contract No. DE-AC5206NA25396. A portion of this work was performed through DOE and NSF grants to Auburn University. The computational work was carried out at the National Institute for Computational Sciences in Oak Ridge, TN. Resources of the Australian National Computational Infrastructure (NCI) Facility and its Western Australian node iVEC are gratefully acknowledged.

[1] J. S. Briggs and V. Schmidt, J. Phys. B **33**, R1 (2000).
[2] A. Knapp *et al.*, Phys. Rev. Lett. **89**, 033004 (2002).
[3] A. S. Kheifets and I. Bray, Phys. Rev. A **73**, 020708 (2006).
[4] J. Ullrich, R. Moshammer, A. Dorn, R. Dörner, L. P. H. Schmidt, and H. Schmidt-Böcking, Rep. Prog. Phys. **66**, 1463 (2003).
[5] P. Bolognesi, A. S. Kheifets, I. Bray, L. Malegat, P. Selles, A. K. Kazansky, and L. Avaldi, J. Phys. B **36**, L241 (2003).
[6] A. Knapp *et al.*, J. Phys. B **38**, 645 (2005).
[7] W. Vanroose, F. Martín, T. N. Rescigno, and C. W. McCurdy, Phys. Rev. A **70**, 050703 (2004).
[8] J. Colgan, M. S. Pindzola, and F. Robicheaux, Phys. Rev. Lett. **98**, 153001 (2007).
[9] T. Weber *et al.*, Phys. Rev. Lett. **92**, 163001 (2004).
[10] M. Gisselbrecht, M. Lavollée, A. Huetz, P. Bolognesi, L. Avaldi, D. P. Seccombe, and T. J. Reddish, Phys. Rev. Lett. **96**, 153002 (2006).
[11] P. Bolognesi *et al.*, Phys. Scr. **2004**, 62 (2004).
[12] P. Bolognesi, R. Flammini, A. Kheifets, I. Bray, and L. Avaldi, Phys. Rev. A **70**, 062715 (2004).
[13] P. Bolognesi, A. Kheifets, S. Otranto, M. Coreno, V. Feyer, F. D. Colavecchia, C. R. Garibotti, and L. Avaldi, J. Phys. B **39**, 1899 (2006).
[14] K. J. Ross, J. B. West, and H.-J. Beyer, J. Phys. B **30**, L735 (1997).
[15] K. J. Ross, J. B. West, H.-J. Beyer, and A. D. Fanis, J. Phys. B **32**, 2927 (1999).
[16] H.-J. Beyer, J. B. West, K. J. Ross, and A. D. Fanis, J. Phys. B **33**, L767 (2000).
[17] J. B. West, K. J. Ross, H.-J. Beyer, A. D. Fanis, and H. Hamdy, J. Phys. B **34**, 4167 (2001).
[18] P. Sheridan, M. Grimm, and E. Sokell, J. Phys. B **41**, 165204 (2008).
[19] L. Malegat, F. Citrini, P. Selles, and P. Archirel, J. Phys. B **33**, 2409 (2000).
[20] F. Maulbetsch, I. L. Cooper, and A. S. Dickinson, J. Phys. B **33**, L119 (2000).
[21] A. S. Kheifets and I. Bray, Phys. Rev. A **65**, 012710 (2001).
[22] F. Citrini, L. Malegat, P. Selles, and A. K. Kazansky, Phys. Rev. A **67**, 042709 (2003).
[23] J. Colgan and M. S. Pindzola, Phys. Rev. A **65**, 022709 (2002).
[24] F. L. Yip, C. W. McCurdy, and T. N. Rescigno, Phys. Rev. A **81**, 053407 (2010).
[25] R. Wehlitz and S. B. Whitfield, J. Phys. B **34**, L719 (2001).
[26] D. Lukic, J. B. Bluett, and R. Wehlitz, Phys. Rev. Lett. **93**, 023003 (2004).

[27] R. Wehlitz, D. Lukic, and J. B. Bluett, Phys. Rev. A **71**, 012707 (2005).
[28] A. S. Kheifets, D. V. Fursa, C. W. Hines, I. Bray, J. Colgan, and M. S. Pindzola, Phys. Rev. A **81**, 023418 (2010).
[29] G. Zhu, M. Schuricke, J. Steinmann, J. Albrecht, J. Ullrich, I. Ben Itzhak, T. J. M. Zouros, J. Colgan, M. S. Pindzola, and A. Dorn, Phys. Rev. Lett. **103**, 103008 (2009).
[30] A. Knapp *et al.* J. Phys. B **35**, L521 (2002).
[31] M. Pont and R. Shakeshaft, Phys. Rev. A **54**, 1448 (1996).
[32] A. S. Kheifets, D. V. Fursa, and I. Bray, Phys. Rev. A **80**, 063413 (2009).
[33] A. T. Stelbovics, I. Bray, D. V. Fursa, and K. Bartschat, Phys. Rev. A **71**, 052716 (2005).
[34] D. A. Varshalovich, A. N. Moskalev, and V. K. Khersonskii, *Quantum Theory of Angular Momentum*, 1st ed. (World Scientific, Philadelphia, 1988).
[35] J. Colgan, D. C. Griffin, C. P. Ballance, and M. S. Pindzola, Phys. Rev. A **80**, 063414 (2009).
[36] J. Colgan, M. S. Pindzola, and F. Robicheaux, J. Phys. B **34**, L457 (2001).
[37] A. S. Kheifets, I. Bray, J. Colgan, and M. S. Pindzola, J. Phys. B (submitted).
[38] A. Dorn (private communication).